Supplementary Information

Submolecular video-imaging of the Smc5/6 complex topologically bound to DNA

Kenichi Umeda[1,2*], Yumiko Kurokawa[3,4], Noriyuki Kodera[1*] and Yasuto Murayama[3,4*]

[1]Nano Life Science Institute (WPI-NanoLSI), Kanazawa University, Kanazawa, Ishikawa, Japan.

[2] PRESTO/JST, 4-1-8 Honcho, Kawaguchi, Saitama, Japan.

[3] Department of Chromosome Science, National Institute of Genetics, ROIS, Mishima, Japan.

[4] Graduate University for Advanced Studies (SOKENDAI), Mishima, Japan.

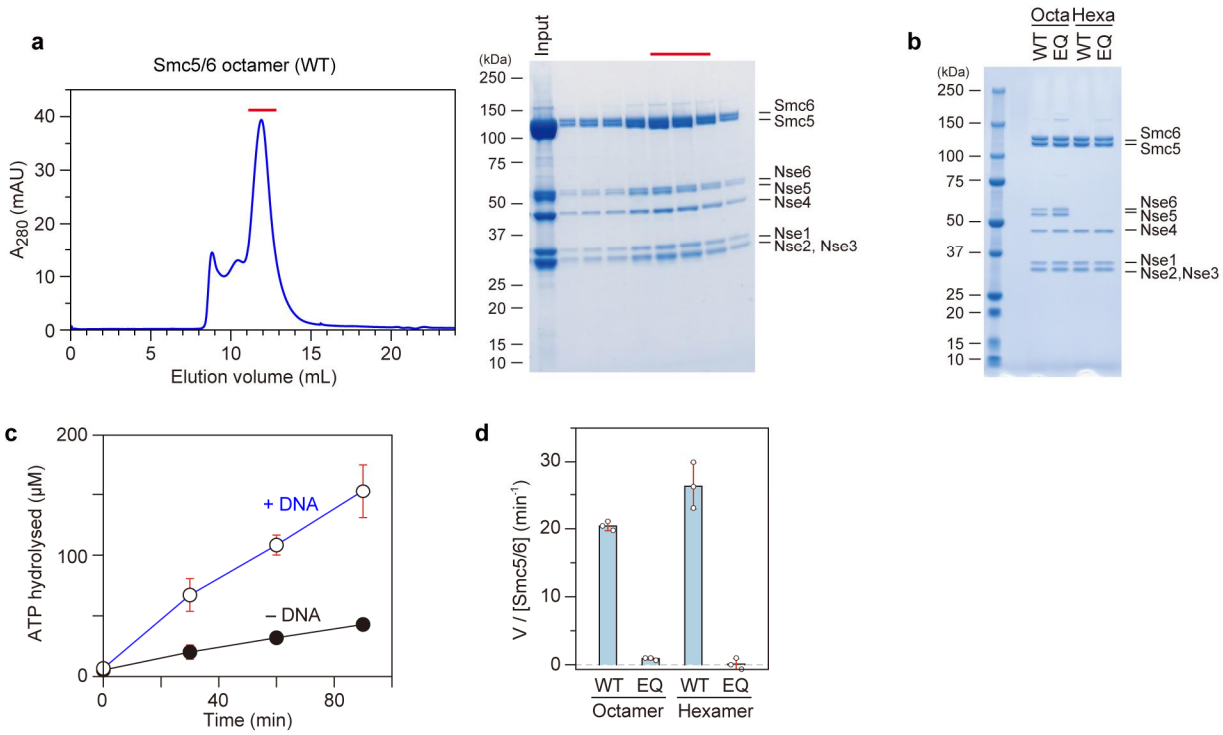

Supplementary Figure 1| Purification of the budding yeast Smc5/6 complex.

a, Size-exclusion chromatogram profile of the Smc5/6 octamer (left). The fractions were analyzed by SDS-PAGE followed by Coomassie brilliant blue (CBB) staining (right). The peak fractions, indicated by red lines, were collected and used for HS-AFM and biochemical analyses.

b, Purified wild-type and EQ mutant Smc5/6 hexamers and octamers were analyzed by SDS-PAGE followed by CBB staining.

c, Time-course of ATP hydrolysis by the Smc5/6 octamer with or without DNA.

d, ATPase activities of the indicated Smc5/6 complexes in the presence of DNA, which were measured from the concentration of phosphate products at the 30-minute time point following the initiation of the reaction. In panels c and d, data are presented as means ± SD. from three independent experiments.

Source data are provided as a source data file.

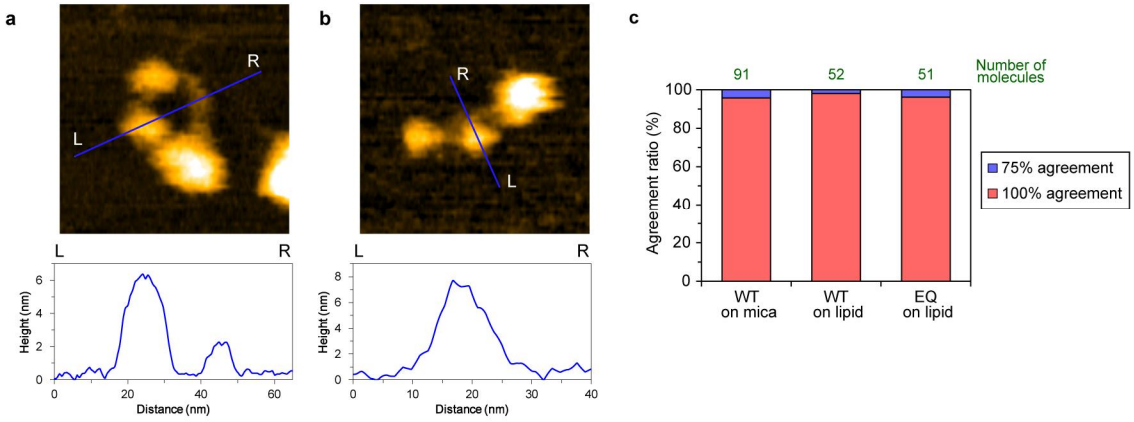

Supplementary Figure 2| Classification of the I- and O-forms

a,b, Representative HS-AFM images of the O-form (a) and I-form (b) (upper panels), and the corresponding line-profile analyses across the Smc5 and Smc6 arms (lower panels). The line profiles revealed a substrate-level minimum (i.e., the mica surface) between the SMC arms in the O-form, which was absent in the I-form.

c, Statistical evaluation of classification agreement for WT molecules observed on mica (analysis of Fig. 1d), and for DNA-bound WT and EQ mutant molecules using the lipid membrane stage (analysis of Fig. 5e). Four independent analysts performed the classification, and agreement rates exceeding 95% were obtained under all conditions, demonstrating the robustness of the classification procedure.

Source data are provided as a source data file.

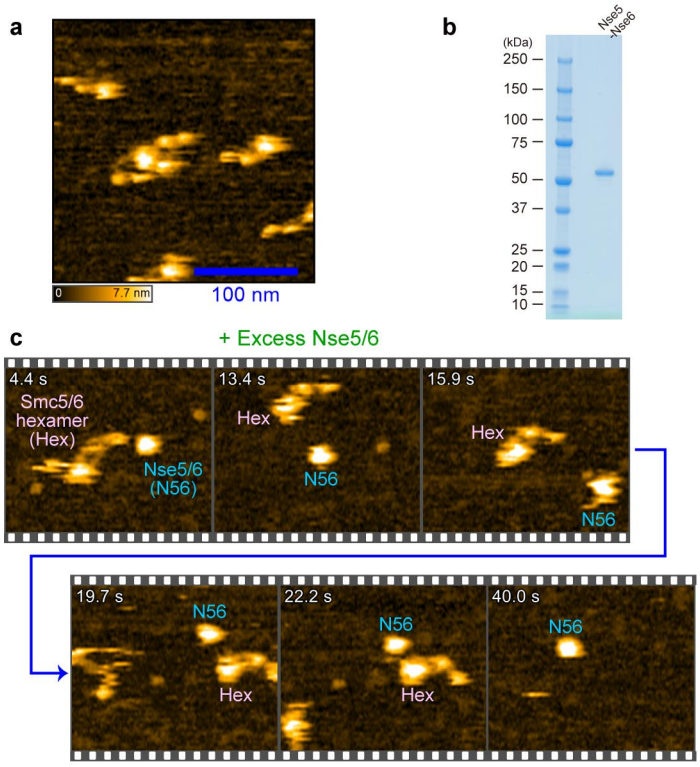

Supplementary Figure 3| HS-AFM observation of the Smc5/6 octamer using a mica imaging stage.

a, HS-AFM observation of the Smc5/6 octamer in a buffer containing 300 mM KOAc. The octamer consists of the Smc5/6 hexamer and the DNA-loading accessory factor, the Nse5–Nse6 heterodimer (Nse5/6). Nse5/6 were co-purified with Smc5/6 hexamer during gel filtration chromatography (Supplementary Fig. 1a), indicating a stable octameric complex in solution. However, after deposition on mica, we predominantly observed 'SMC'-shaped molecules corresponding to the Smc5/6 hexamer state (Fig. 1a). Scan area, 250 × 250 nm^2 at 200 × 100 $pixels^2$. Imaging rate: 1.3 s per frame.

b, Purification of the Nse5/6 heterodimer. Purified Nse5/6 was analyzed by SDS-PAGE followed by CBB staining.

c, Nse5/6 appeared to dissociate from the Smc5/6 core complex when placed on mica. We observed the Smc5/6 octamer after the addition of excess amounts of the purified Nse5/6. Adsorption of Nse5/6 on mica was seen when 10-fold excess amounts of Nse5/6 compared to Smc5/6 octamer was applied. This suggests that Nse5/6 was not stably adsorbed on mica and was prone to detachment. Under these conditions, we occasionally observed Smc5/6 molecules corresponding to the hexamer state (Hex) and Nse5/6 (N56) in the same viewing window, but they never physically interacted with each other. These results strongly suggest that when the Smc5/6 octamer was placed on mica, the physical interaction between the Smc5/6 hexamer and Nse5/6 became unstable. Consequently, the Nse5/6 dissociated from the Smc5/6 hexamer and detached from mica, preventing visualisation of the Smc5/6 octamer under the current experimental conditions. Due to this limitation, this study focused on the hexamer for the visualisation of the Smc5/6 complex.

Scan area, 200 × 120 nm^2 at 200 × 60 $pixels^2$, cropped to 150 × 120 nm^2. Imaging rate: 0.63 s per frame.

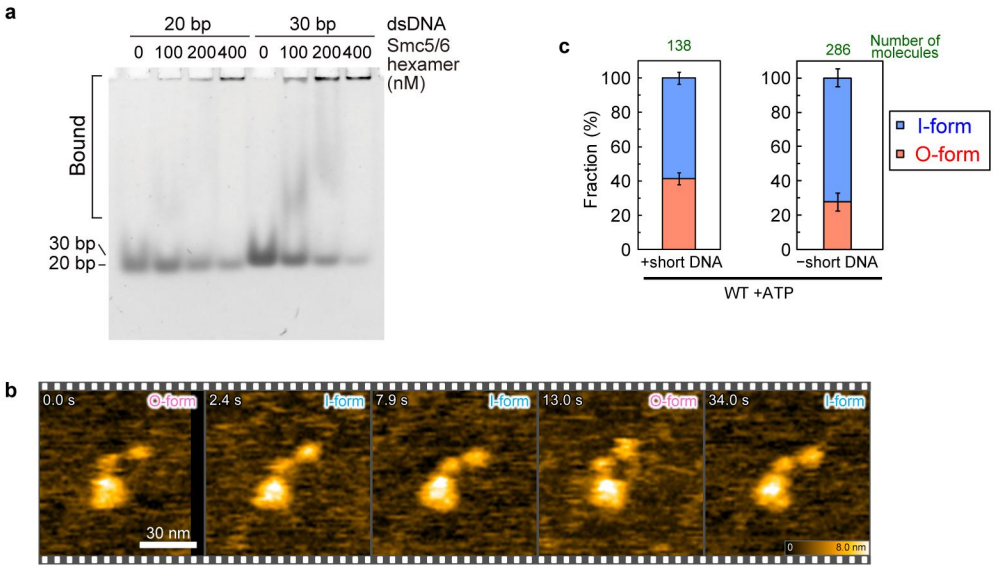

Supplementary Figure 4| Effect of Short DNA on the Conformation of Smc5/6

a, Binding of Smc5/6 to short double-stranded DNA (20 bp and 30 bp) was analyzed using an electrophoretic mobility shift assay (EMSA).

b, HS-AFM imaging of Smc5/6 hexamers in the presence of an excess amount of 20-bp short DNA. Scan area, 120 × 120 nm^2 at 80 × 80 $pixels^2$, cropped to 102 × 102 nm^2. Imaging rate, 0.34 s per frame.

c, Abundance ratios of I- and O-forms in the presence of 20-bp DNA calculated from individual molecules (obtained from three independent experiments), where error bars represent SEM. The data obtained without DNA from Fig. 1d is shown for comparison.

Source data are provided as a source data file.

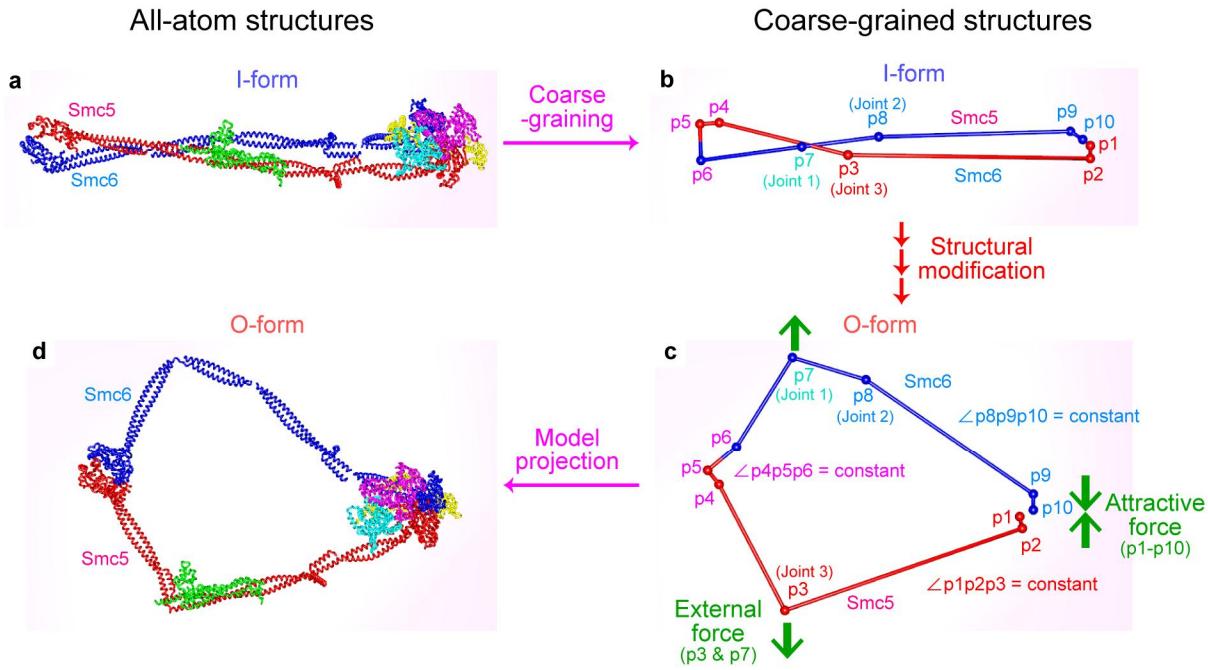

Supplementary Figure 5| Atomic model construction of the ATP-bound Smc5/6 hexamer.

a, The atomic model of apo-state Smc5/6 complex from cryo-EM structure (PDB-7QCD).

b, A coarse-grained (CG) framework generated from **a**. As described in Methods, we placed 10 CG-particles (denoted as p) at the following amino-acid residues, which were connected by 9 rigid chains: E187 (p1) and T200 (p2) on the Smc5 ATPase head, D739 (p3) on the Smc5 arm, Q647 (p4) and N618 (p5) on the Smc5 head, N503 (p6) on the Smc6 hinge, V761 (p7) and I805 (p8) on the Smc6 arm, and T1035 (p9) and S229 (p10) on the Smc6 ATPase (see also Supplementary Table 1). The ATPase head regions were defined as E187 (p1) – T200 (p2) for Smc5 and S229 (p10) – T1035 (p9) for Smc6, as these residues are almost linearly aligned in the atomic model of the ATP bound Smc5/6 hexamer derived from the cryo-EM structure (PDB-7TVE).

c, Conversion of the I-form framework to the O-form. The I-form framework was converted to the O-form by applying virtual pulling forces at the middle of SMC arms (p3 and p7) in opposite directions. In this framework model, we fixed the angles of pairs of two chains defined as S1 (p1-p2-p3), S3 (p4-p5-p6) and S6 (p8-p9-p10) (Supplementary Table 2). A harmonic oscillator model-type force was also applied between p1 and p10 to recapitulate the ATP-dependent heads engagement, maintaining the p1–p10 distance at 1.2 nm.

d, The predicted atomic structure of the ATP-bound Smc5/6 complex. The atomic model of the ATP-bound form was generated by projecting the apo-state atomic model onto the coordination of the coarse-grained model of the O-form for each part.

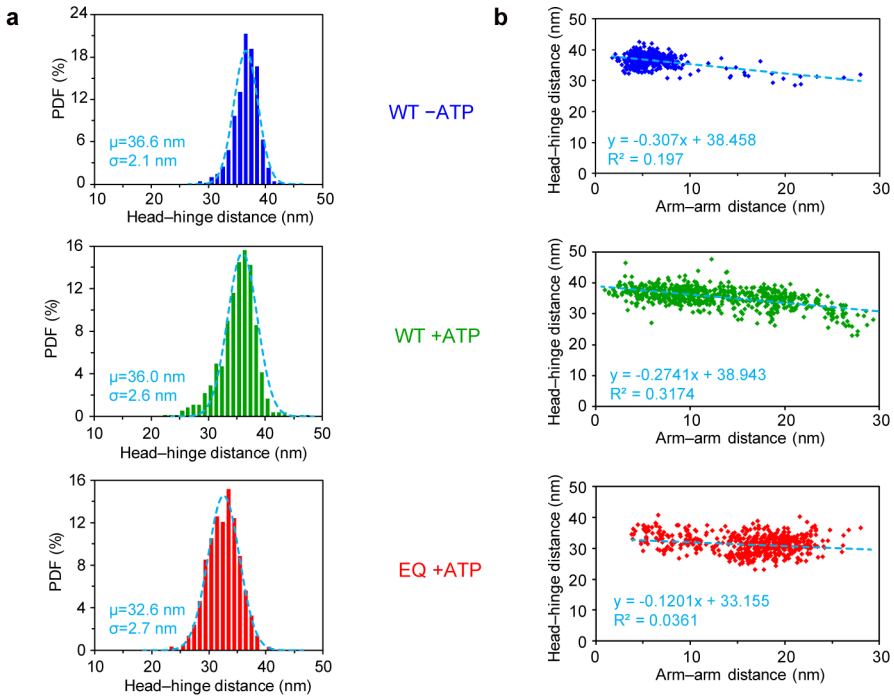

Supplementary Figure 6| Quantification of the head–hinge distance.

a, Distribution of head–hinge distances extracted from the data in Fig. 3c. The mean (μ) and standard deviation (σ) obtained by Gaussian fitting are shown in the graph.

b, Correlation between the arm–arm and head–hinge distances. The linear regression equation and the R^2 value obtained by linear fitting are shown in the graph.

The head–hinge distances remained almost constant, regardless of the corresponding arm–arm distances, in WT with or without ATP. The EQ mutant showed 11% decrease in the head–hinge distance compared with WT. By contrast, the I-form showed 53% decrease in the arm–arm distance as compared with that of O-form (Fig. 3). These results demonstrate that head-hinge distances are not correlated with the degrees of corresponding arm-arm distances, and that this value is not applicable to distinguish the molecular shape of Smc5/6 quantitatively.

Source data are provided as a source data file.

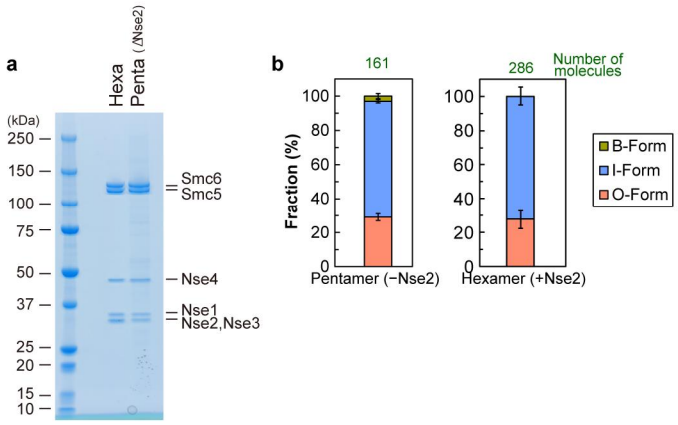

Supplementary Figure 7| Purification of Smc5/6 lacking Nse2 (pentamer).

a, Purified Smc5/6 pentamer along with the hexamer were analyzed by SDS-PAGE followed by CBB staining.

b, Abundance ratios of different conformations calculated from the individual pentamer molecules observed in the presence of ATP (obtained from three independent experiments), where error bars represent SEM. The data for the hexamer (+Nse2) from Fig. 1d is shown for comparison.

Source data are provided as a source data file.

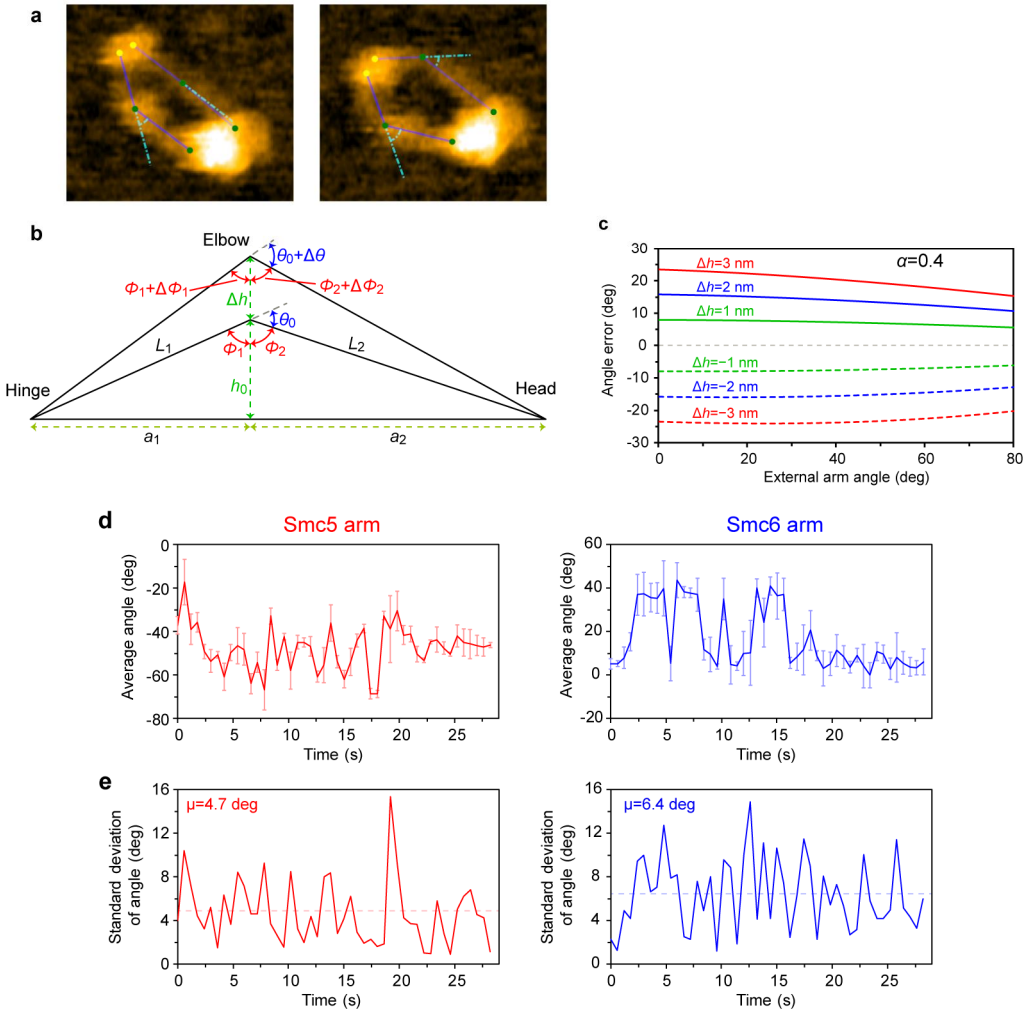

Supplementary Figure 8| Quantification of the bending angles at the Smc5/6 arms.

a, Measurement of SMC arm bending angles. For each SMC arm, a two-segment ridge line was placed connecting the hinge to the head. The yellow and green dots indicate the control points corresponding to the hinge domain and other domains, respectively. The bending angle was then measured at the junction between the two segments (see Methods).

b, Theoretical framework for calculating errors in SMC arm angle measurements (see below for details).

c, Estimation of angular errors using the framework shown in (b) under different parameter settings.

d, Real-time traces of SMC elbow angles measured by three independent analysts using the same dataset of 100 frames. The graph shows the average elbow angles measured by the three analysts (authors of this study). Error bars represent the standard deviation.

e, The standard deviation at each time points was plotted. The means standard deviation (μ, dash-lines) for the Smc5 and Smc6 are 4.7 and 6.4 degrees, respectively.

Source data are provided as a source data file.

For the measurements of SMC arm bending angles, we manually drew two straight lines along each SMC arm in each frame to determine the elbow angle (Supplementary Fig. 8a). For Smc5, three control points were placed at the head, hinge, and Nse2 positions, and these points were used to define two straight segments, from which the intersection angle was calculated. For Smc6, two control points were placed at the head and hinge. The third control point was placed on the curved region of its arm. As shown in Fig. 2, our simulation showed that the O-form conformation can be induced by bending the Smc6 arm at the Joint 1 elbow, which is located at a 40:60 ratio relative to the hinge-elbow and elbow-head. We placed the control points according to this ratio. In some frames, the Smc6 arm appeared straight, and the curvature of the arm was not clearly visible. In such cases, we positioned the control point on the SMC6 arm at a ratio of 40:60 relative to the hinge-elbow and elbow-head joints.

When the arm length is sufficiently large compared with its widths, the defined angle is uniquely determined. In actual HS-AFM images, however, the finite arm widths, measurement noise, and slight asymmetry of the cross-sectional height profile can introduce some uncertainty in the placement of control points. Below, we therefore provide a theoretical estimate of the angular error arising from these factors.

The arm length of Smc5 and Smc6 is approximately 30 nm, and the elbows are estimated to located at 43:57 for Smc5 and 40:60 ratio for Smc6 relative to the hinge-elbow and elbow-head, respectively, based on our molecular simulation shown in Fig. 2. Thus, as illustrated in Supplementary Fig. 8a, we approximate the lines connecting the hinge–elbow–head points as forming a scalene triangle. If the total arm length is denoted by L_0, the lengths of the two segments, L_1 (hinge–elbow) and L_2 (elbow–head), are expressed as follows.

$$\begin{aligned} L_1 &= \alpha L_0, \\ L_2 &= (1-\alpha) L_0, \end{aligned} \tag{1}$$

where α represents the relative position of the elbow along the arm, corresponding to values of α=0.43 and α=0.40, for Smc5 and Smc6 arms, respectively.

At this point α, we define the base lengths as a_1 and a_2, and the height as h_0. If the apex angle, divided by the two sides L_1 and L_2, is denoted by ϕ_0, and the two resulting angles produced by the perpendicular height are ϕ_1 and ϕ_2, respectively, the following relationship holds:

$$\phi_0 = \phi_1 + \phi_2. \tag{2}$$

Although we quantify the *external* elbow angle in the HS-AFM analyses, the *internal* angle is more convenient for the theoretical derivation. The external angle θ_0 and the internal angle ϕ_0 are related by:

$$\phi_0 = \pi - \theta_0. \tag{3}$$

Geometrically, the height h_0 can be expressed as:

$$h_0 = L_1 \cos\phi_1 = L_2 \cos\phi_2 \tag{4}$$

By applying the addition theorem to decompose the third term, we obtain:

$$L_1 \cos\phi_1 = L_2 \left(\cos\phi_0 \cos\phi_1 + \sin\phi_0 \sin\phi_1\right) \tag{5}$$

Solving this expression for ϕ_1 yields:

$$\phi_1 = \tan^{-1}\left(\frac{\frac{\alpha}{1-\alpha} - \cos\phi_0}{\sin\phi_0}\right) \tag{6}$$

$$\phi_2 = \phi_0 - \phi_1 \tag{7}$$

Furthermore, a_1 and a_2 are given by:

$$\begin{aligned} a_1 &= L_1 \sin(\phi_1), \\ a_2 &= L_2 \sin(\phi_2). \end{aligned} \tag{8}$$

Next, we consider the case in which the control points are placed manually. Let Δh represent the maximum positional error in locating the elbow, and let $\Delta\phi$ denote the resulting angular error. Geometrically, the elbow angle is then expressed as:

$$\phi_1 + \Delta\phi_1 = \tan^{-1}\left(\frac{a_1}{h_0 + \Delta h}\right), \tag{9}$$

$$\phi_2 + \Delta\phi_2 = \tan^{-1}\left(\frac{a_2}{h_0 + \Delta h}\right), \tag{10}$$

By combining these results, we obtain the following equation:

$$\begin{aligned} \Delta\theta &= -\Delta\phi_1 - \Delta\phi_2 \\ &= \phi_0 - \tan^{-1}\left(\frac{\sin\phi_1}{\cos\phi_1 + \frac{\Delta h}{\alpha L_0}}\right) - \tan^{-1}\left(\frac{\sin\phi_2}{\cos\phi_2 + \frac{\Delta h}{(1-\alpha)L_0}}\right). \end{aligned} \tag{11}$$

When we substituted L_0=30 nm and α=0.4 (the elbow position of Smc6) into this equation and plotted the result, we found that the error strongly depends on Δh. The error also shows a slight decreasing trend as θ_0 increases. Since the full width at half maximum (FWHM) of SMC arms in AFM images is approximately 8 nm, we consider Δh=1−2 nm to be a reasonable estimate (Supplementary Fig. 8c). Therefore, the angular error is estimated to be approximately 8°–16°.

Aside from the theoretical estimations, we also measured the arm angles by three independent analysts using same dataset to calculate the range of measuring errors (Supplementary Fig. 8d). From these data, we calculated the means of standard deviations, which were 4.7° for Smc5 and 6.4° for Smc6. Accordingly, twice the standard deviation, corresponding to the 95% error range, was approximately 13° for both Smc5 and Smc6, which was consistent with the theoretical estimation described above. Although measuring the arm angle involves a certain degree of error, the range is similar for both Smc5, which has Nse2, and Smc6. Therefore, we concluded that the arm angle is measured with a similar level of accuracy for both SMC arms.

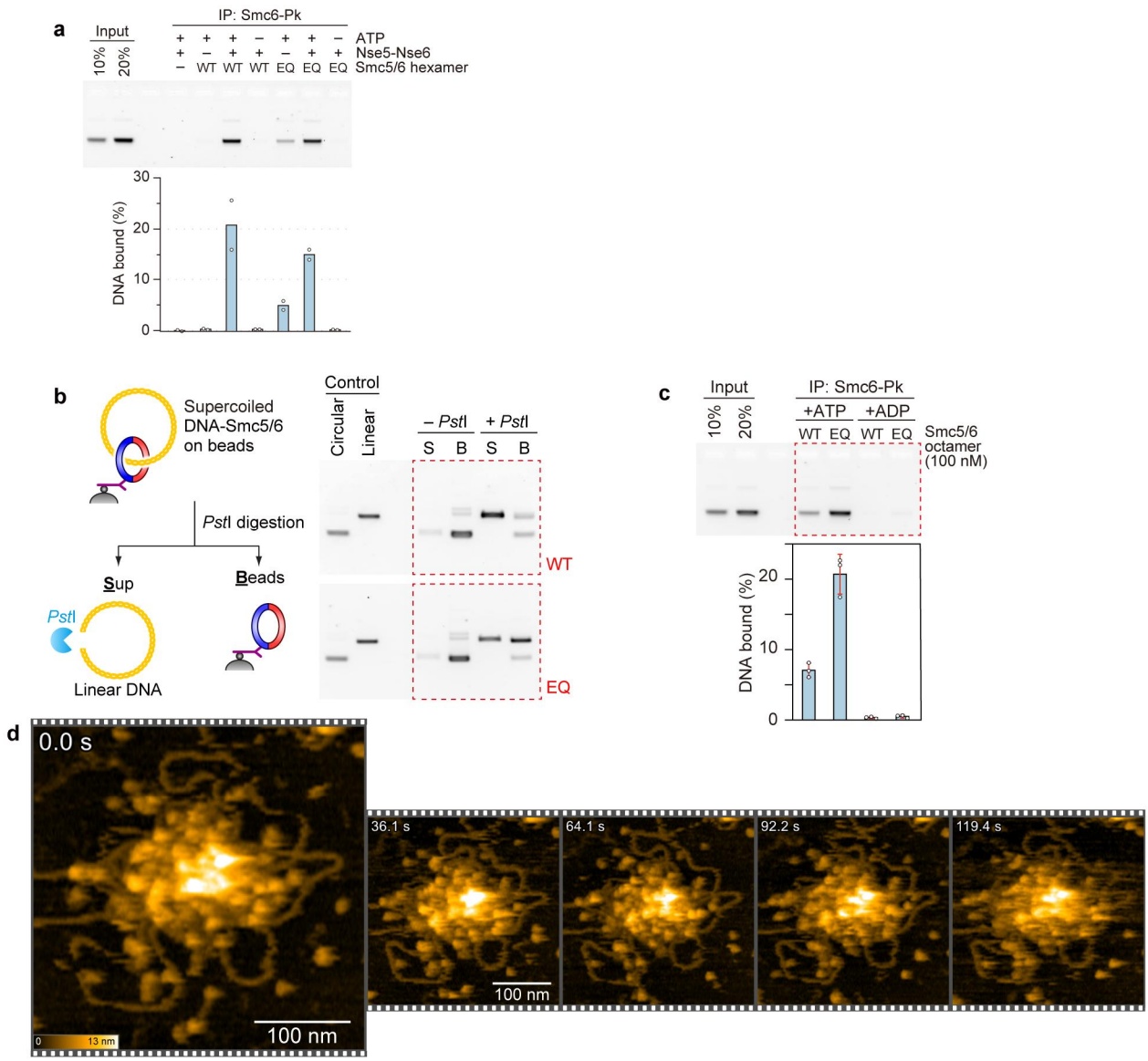

Supplementary Figure 9| Biochemical reconstitution of topological DNA entrapment by Smc5/6.

a, Agarose gel analysis of the DNA loading experiment using the Smc5/6 hexamer and separately purified Nse5-Nse6. Efficient DNA recovery was seen only when Nse5-Nse6 was added in the presence of ATP.

b, Schematic and gel images of the DNA-release experiments using restriction digestion to confirm the topological nature of DNA loading. Smc5/6 was initially loaded onto supercoiled plasmid DNA in the presence of ATP as **a**. After immunoprecipitation and high-salt washing to retrieve Smc5/6, the Smc5/6-bound DNA was digested with restriction enzyme *Pst*I. The cleaved DNA was released into the supernatant, while undigested DNA remained in the Smc5/6-bound bead fraction. This result indicates that linearized DNA was able to escape from Smc5/6.

c, Same as Fig 4b, except that the experiment was carried out using the EQ mutant octamer complex in addition to the wild-type.

d, Successive HS-AFM images of DNA-bound Smc5/6 using a mica imaging stage under a buffer with a low concentration of KOAc. Scan area, 400 × 400 nm^2 at 240 × 120 $pixels^2$. Imaging rate: 0.8 s per frame.

Source data are provided as a source data file.

Since both mica and DNA are negatively charged, DNA cannot be adsorbed on mica without modifying the surface. This can be achieved by using an imaging buffer containing potassium ions, with a salt concentration of approximately several tens of mM. Under these conditions multiple Smc5/6 molecules were found to stack on the DNA. Additionally, free Smc5/6 molecules could also be adsorbed onto the mica surface, making it difficult to distinguish DNA-bound Smc5/6 from free molecules adsorbed near the DNA. Therefore, we used the lipid membrane stage system to specifically observe DNA-bound Smc5/6 using HS-AFM.

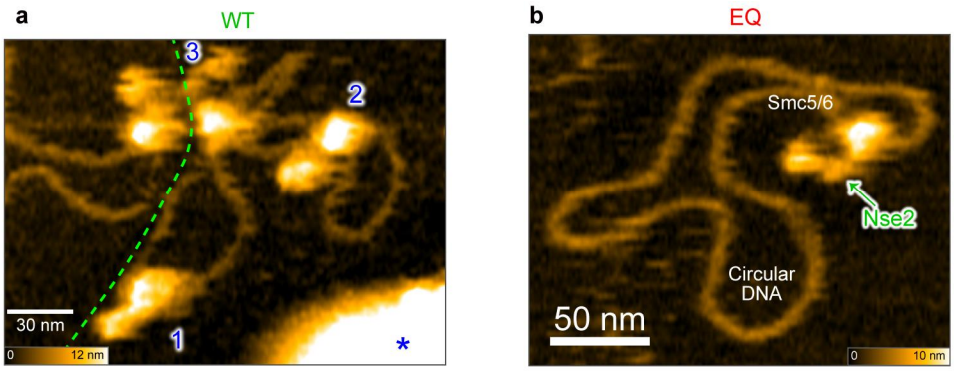

Supplementary Figure 10| Examples of multiple wild-type and single EQ Smc5/6 bound to DNA using a lipid membrane stage system.

a, HS-AFM images showing DNA molecules bound by multiple wild-type Smc5/6 molecules. The green dashed line indicates the boundary between the two DNA molecules, and only those loaded onto the DNA on the right are numbered. Scan area, 250 × 200 nm^2 at 200 × 80 $pixels^2$, cropped to 208 × 150 nm^2. Imaging rate: 0.7 s per frame.

b, Overview scans of the DNA-bound EQ mutant Smc5/6 molecule (Supplementary Movie 4b). Scan area, 300 × 240 nm^2 at 240 × 96 $pixels^2$, cropped to 200 × 156 nm^2. Imaging rate, 1 s per frame.

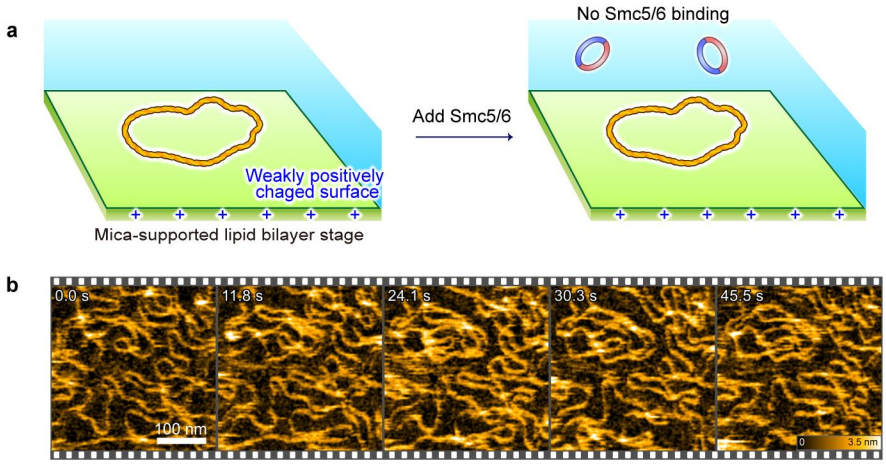

Supplementary Figure 11| Free Smc5/6 molecule does not bind to DNA pre-adsorbed on the lipid membrane.

a, Schematic of the experiment, in which DNA was first adsorbed onto the lipid membrane, followed by the addition of Smc5/6 octamer to the imaging chamber.

b, Successive HS-AFM images of the experiment as **a**. HS-AFM imaging was initiated 3-min after addition of Smc5/6 octamer. DNA substrates, but not protein signals, were seen over time. Scan area, 350 × 350 nm^2 at 120 × 120 $pixels^2$, cropped to 332 × 332 nm^2. Imaging rate, 0.56 s per frame.

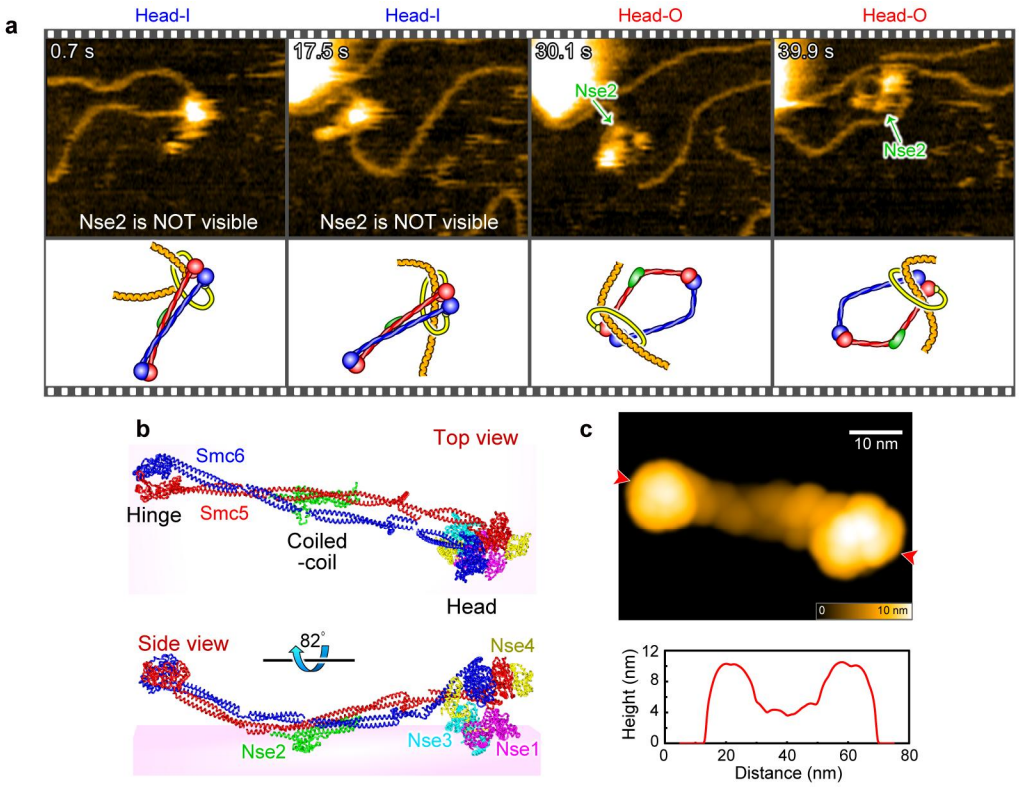

Supplementary Figure 12| DNA-bound Head-I Smc5/6 was adsorbed on the lipid membrane stage in an orientation distinct from that on mica.

a, HS-AFM images showing the transition of DNA-bound Smc5/6 from the I-form to the O-form. In the first two frames, DNA-bound Smc5/6 exhibited the I-form structure; however, unlike the results obtained on mica, Nse2 was not detected on the Smc5 arm. In contrast, the Nse2 signal appeared when the I-form was converted to the O-form in the 30.1 s frame.

b, Atomic model of the budding yeast Smc5/6 hexamer in the apo state derived from cryo-EM structure (EMD-13895, PDB-7QCD), adsorbed onto the surface in the orientation opposite to that shown in Fig. 2b, with Nse2 facing down.

c, A pseudo-AFM image of the Smc5/6 hexamer from panel **b**. In contrast to Fig 2b, Nse2 was not visible in the middle of the SMC arm region. The corresponding line profile of the molecular height across the two red arrowheads is presented. These results suggest that the DNA-bound I-form of Smc5/6 was adsorbed on the lipid membrane surface with Nse2 facing downwards, in contrast to its orientation on mica.

Source data are provided as a source data file.

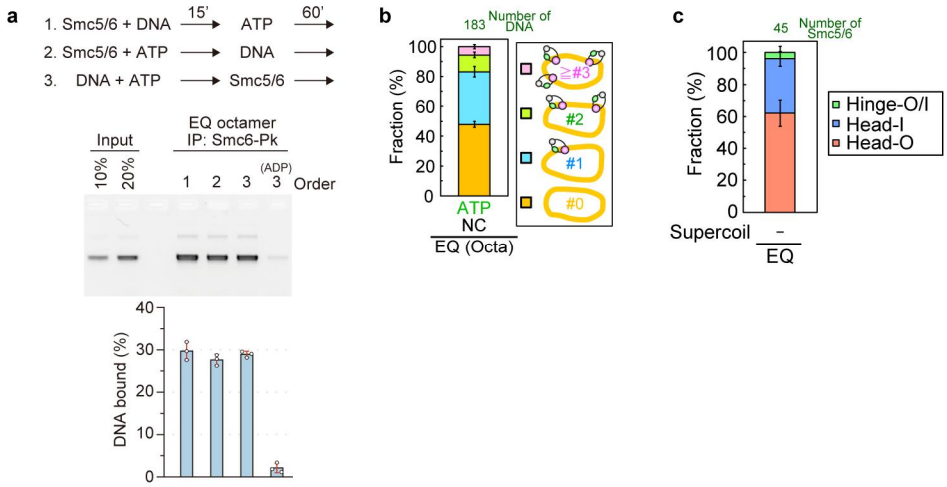

Supplementary Figure 13| ATP preincubation does not alter DNA loading of the ATP hydrolysis-deficient EQ mutant.

a, Bulk DNA loading experiments were carried out in the order of addition indicated. Representative gel images and quantifications of loading assays using the Smc5/6 EQ mutant octamer are shown (means of three independent experiments ± SD.).

b, Quantification of DNA-bound Smc5/6 EQ mutant observed by HS-AFM using the lipid membrane stage (means of three independent experiments ± SEM.). The EQ mutant was preincubated with ATP for 30 min prior to DNA addition (Order 2 in **a**). After a 120-min incubation, the reaction mixture was applied to the lipid stage for HS-AFM imaging.

c, Abundance ratios of Smc5/6 EQ mutant conformations bound to DNA, derived from the ATP preincubation experiment (means of three independent experiments ± SEM.).

Source data are provided as a source data file.

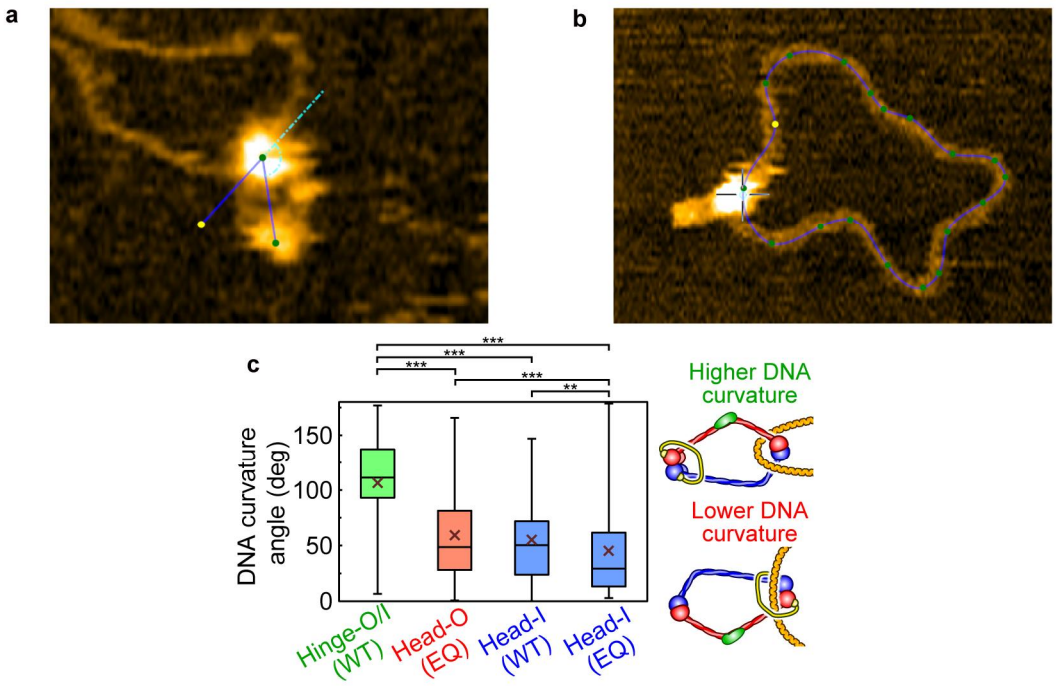

Supplementary Figure 14| Smc5/6 binding at the hinge or head exhibits distinct molecular behaviours on DNA.

a, Measurements of Smc5/6 binding angles relative to DNA (see Methods).

b, Measurements of DNA curvature angles at Smc5/6 binding sites (see Methods). The cross-hair indicates the anchor point corresponding to the molecular binding site.

c, Quantification of DNA curvature angles, based on a total of 165, 236, 147, and 143 frames for WT Hinge-O/I, WT Head-O, WT Head-I, and EQ Head-I, respectively (n = 3 molecules per condition) from successive HS-AFM images. In the box plots, the centre line represents the median, the crosses indicate the mean values, the lower and upper bounds of the box represent the 25th and 75th percentiles, respectively, and the whiskers extend to the minimum and maximum values. Statistical differences were assessed using the two-sided nonparametric Brunner-Munzel test (***: $p < 0.001$). The Brunner–Munzel test was used to compare two independent groups without assuming equal variances or identical distributional shapes.

Source data are provided as a source data file.

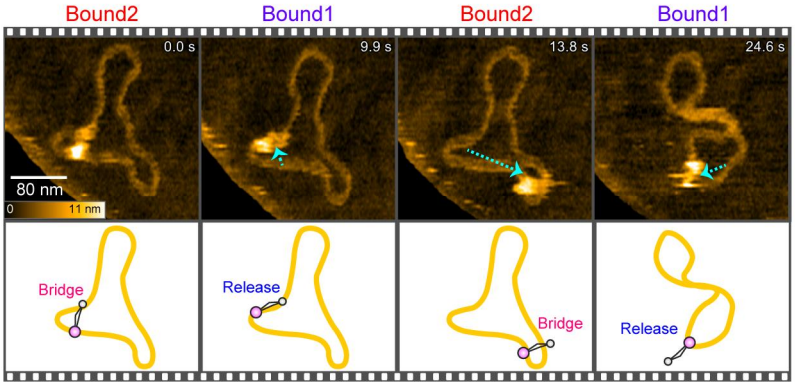

Supplementary Figure 15| Transient DNA bridging by Smc5/6 in the "Bound 2 (bridge)" state.
Successive HS-AFM images of Smc5/6 bound DNA in the "Bound 2" state. Smc5/6 repeatedly bridged two DNA segments and released one of them during HS-AFM observation. Based on these results, we concluded that the DNA bridging observed in the "Bound 2" state was transient. Scan area, 350 × 280 nm^2 at 200 × 80 $pixels^2$, cropped to 280 × 250 nm^2. Imaging rate: 0.98 s per frame.

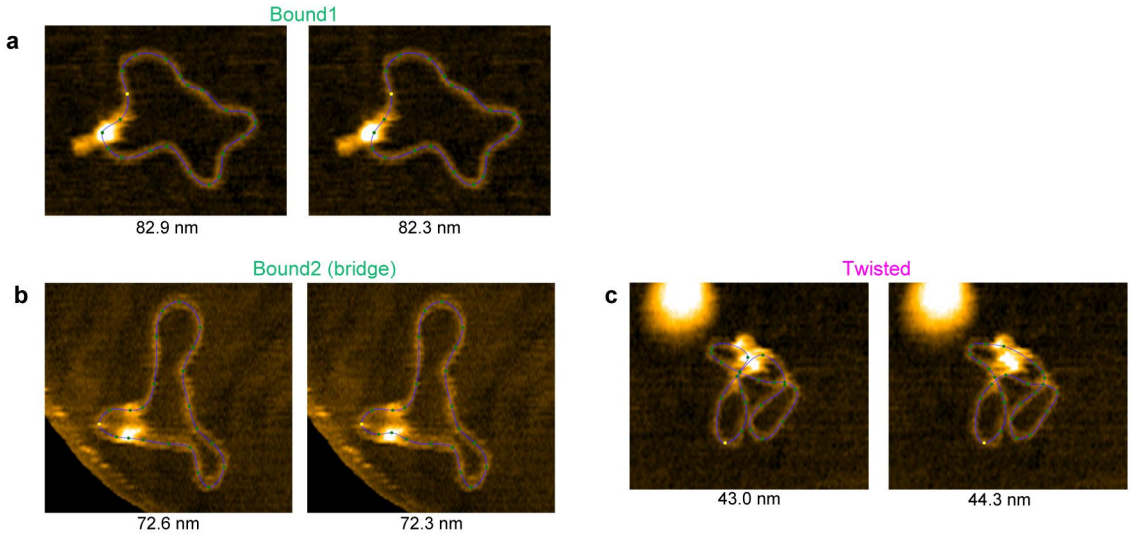

Supplementary Figure 16| Radius of gyration (R_g) analysis of DNA using different line trajectories in the Smc5/6-bound region.

a–c, Comparison of R_g values calculated using two different line trajectories in the Smc5/6-bound region from the same HS-AFM images. The Bound1 (a), Bound2 (bridge) (b), and Twisted (c) conformations shown in Fig. 6a are analyzed. To calculate the R_g of Smc5/6-bound DNA, control points were manually placed along the DNA contour, and a spline-interpolated line was generated. The actual DNA trajectory became ambiguous in regions bound by Smc5/6, particularly in the Twisted species. To estimate this uncertainty, R_g was calculated using two different sets of control-point placements in the Smc5/6-bound regions, yielding an estimated error of ~3%.

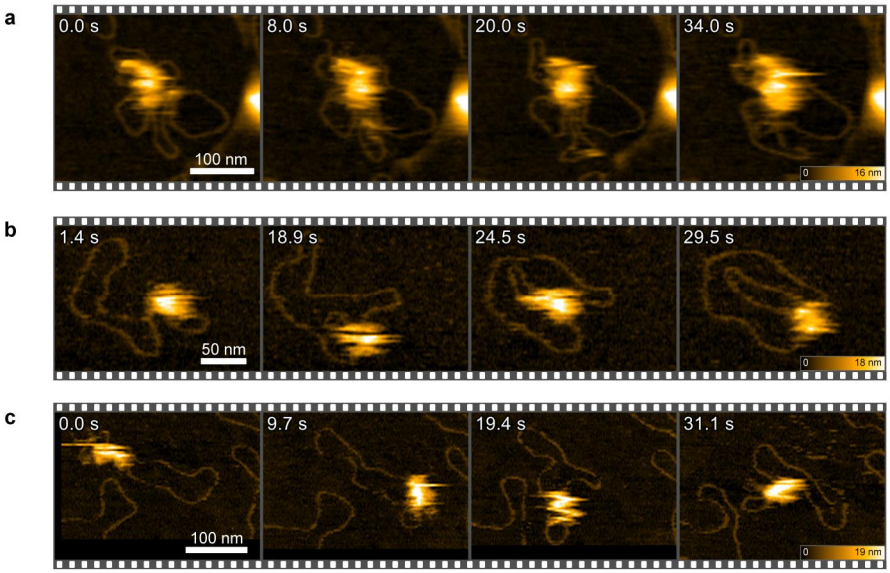

Supplementary Figure 17| Stabilization of the Twist Structure by Smc5/6 oligomer

a, Successive HS-AFM images of twisted DNA species bound by multiple Smc5/6 molecules forming a cluster. Smc5/6 exhibited persistent interactions with DNA across multiple consecutive frames (Supplementary Movie 7a).

b,c, Smc5/6 clusters tethered two DNA strands and displayed coordinated movement. Two representative examples are shown (Supplementary Movie 7b,c).

a, Scan area, 400 × 400 nm^2 at 240 × 120 $pixels^2$, cropped to 320 × 260 nm^2. Imaging rate, 1 s per frame.

b, Scan area, 350 × 280 nm^2 at 240 × 96 $pixels^2$, cropped to 332 × 238 nm^2. Imaging rate, 0.97 s per frame.

c, Scan area, 250 × 200 nm^2 at 200 × 80 $pixels^2$, cropped to 225 × 160 nm^2. Imaging rate, 0.7 s per frame.

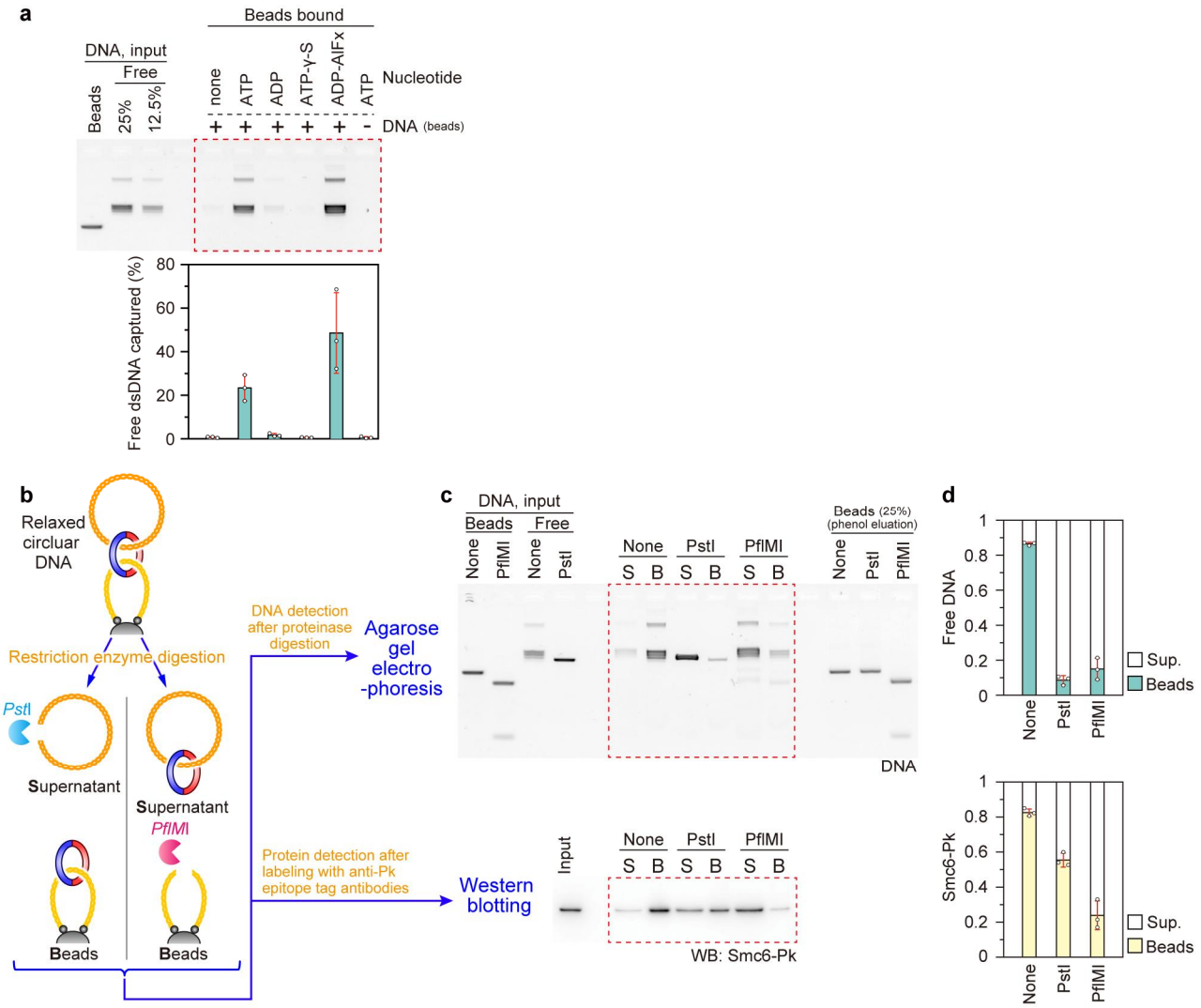

Supplementary Figure 18| Smc5/6 mediates DNA–DNA tethering through topological DNA entrapment.

a, Representative agarose gel image of the DNA–DNA tethering assay in the absence or presence of the indicated nucleotide derivatives. The graph shows the quantification of captured free DNA (obtained from three independent experiments; mean ± SD.).

b, Schematic of DNA-release experiments mediated by restriction digestion. After retrieving DNA–DNA tethering products as depicted in Fig. 6d, captured free DNA and DNA immobilized on the magnetic beads was digested by *Pst*I and *Pfl*MI restriction enzymes, respectively. The captured free DNA is expected to be released into the supernatant if DNA–DNA tethering requires topological entrapment. Likewise, digestion of bead-bound DNA would also release Smc5/6 into the supernatant. Afterward, electrophoresis and western blotting were performed.

c, Representative agarose gel (top) showing free DNA tethered by Smc5/6 to immobilized DNA, and western blot (bottom) detecting DNA-bound Smc5/6, described in panel **b**.

d, Quantification of captured free DNA (top) and Smc5/6 bound to DNA beads (bottom) (n = 3 independent experiments; mean ± SD). The majority of captured free DNA was released from immobilized DNA beads

by digestion of free or bead-bound DNA. In addition, a significantly larger amount of Smc5/6 was released into the supernatant upon linearisation of bead-bound DNA. These results strongly suggest that Smc5/6 mediates DNA–DNA tethering.

Source data are provided as a source data file.

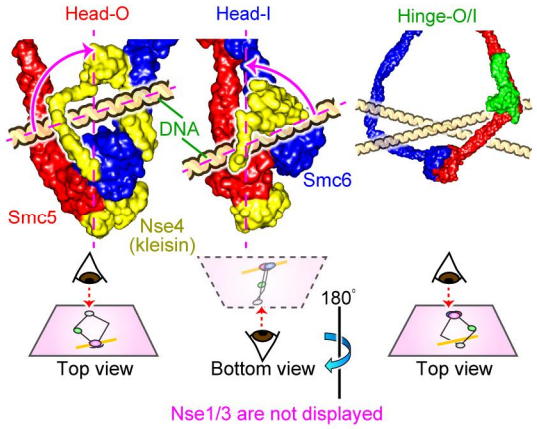

Supplementary Figure 19| Predicted molecular models of Smc5/6 that topologically entrap DNA.
Structural models of the DNA entrapment state of Smc5/6. Left: Head-O, middle: Head-I, right: Hinge-O/I. In the Head-O and Head-I models, DNA strands were positioned within the Nse4 kleisin compartment at the tilt angles observed in our HS-AFM experiments (Fig. 5f), and then fitted into the tilted gap between the kleisin and head domains. Motion of DNA within the Nse4 kleisin appears to be constrained due to the narrower space in the Head-I state, compared to the Hinge-O/I state.

Supplementary Table

Table S1 Assignment of atomic numbers to beads for FJC model construction.

CG-Particle Name	Residue Sequence Number	Atom Serial Number in PDB-7QCD	Subdomain Name	Function Name
p1	E187	1202	Smc5	ABC Domain
p2	T200	1309	Smc5	Head
p3	D739	5649	Smc5	Elbow
p4	Q647	4883	Smc5	Hinge
p5	N618	4647	Smc5	Hinge
p6	N503	11495	Smc6	Hinge
p7	V761	13610	Smc6	Elbow
p8	I805	13951	Smc6	Elbow
p9	T1035	15728	Smc6	Head
p10	S229	9453	Smc6	ABC Domain

Table S2 Assignment of residue numbers to parts for FJC model construction.

Part Name	CG-Particle Range	Residue Sequence Range	Subdomain Name
S1	p1-p2-p3	1–369	Smc5
		738–1068	Smc5
		1–267	Nse2
		1–336	Nse1
		1–303	Nse3
		125–402	Nse4
S2	p3-p4	370–450	Smc5
		648–737	Smc5
S3	p4-p5-p6	451–647	Smc5
		503–692	Smc6
S4	p6-p7	436–502	Smc6
		693–759	Smc6
S5	p7-p8	371–435	Smc6
		760–813	Smc6
S6	p8-p9-p10	1–370	Smc6
		814–1104	Smc6
		1–124	Nse4

Supplementary Note 1

DNA-bound Smc5/6 occasionally underwent relatively long-range translocation within only a few frames, as shown in Supplementary Movie S6. We interpret these abrupt displacements as follows. In our lipid-membrane stage system, the membrane surface is weakly positively charged, allowing DNA segments to adsorb weakly through electrostatic interactions. Consequently, a DNA segment can transiently detach from the membrane surface. Because Smc5/6 exhibits little or no interaction with the lipid membrane itself, when the DNA segment carrying Smc5/6 lifts off the surface, the complex can undergo rapid lateral diffusion. If this motion occurs within a time interval shorter than the HS-AFM frame acquisition time, it can appear as an instantaneous long-range displacement between consecutive frames. Indeed, during the long-distance displacement observed between 50.9 and 51.9 s, the DNA segment spanning the initial and final positions of Smc5/6 appeared transiently distorted in Supplementary Movie S6. These observations are consistent with Smc5/6 remaining continuously associated with the DNA throughout this event rather than dissociating and rebinding.